Hindawi
Shock and Vibration
Volume 2018, Article ID 7476387, 11 pages
https://doi.org/10.1155/2018/7476387

Research Article

A New Approach to Achieve Variable Negative Stiffness by Using an Electromagnetic Asymmetric Tooth Structure

Chao Han,[1] **Xueguang Liu**,[1] **Muyun Wu**,[1] **and Weilong Liang**[2]

[1]*College of Power and Energy Engineering, Harbin Engineering University, Harbin 150001, China*
[2]*Powertrain Global R&D Center, Changan Automobile Co. Ltd., Chongqing 400000, China*

Correspondence should be addressed to Xueguang Liu; liuxueguang2014@hotmail.com

Received 5 December 2017; Revised 18 April 2018; Accepted 30 April 2018; Published 30 May 2018

Academic Editor: Mahmoud Bayat

Traditional passive nonlinear isolators have been paid much attention in recent literatures due to their excellent performance compared to linear vibration isolators. However, they are incapable of dealing with varying conditions such as changing excitation frequency due to the nonadjustable negative stiffness. To solve this drawback, a new approach to achieve variable negative stiffness is proposed in this paper. The negative stiffness is realized by an electromagnetic asymmetric magnetic tooth structure and can be changed by adjusting the magnitude of the input direct current. Analytical model of the electromagnetic force is built and simulations of magnetic field are conducted to validate the negative stiffness. Then the EATS is applied to vibration isolation and an electromagnetic vibration isolator is designed. Finally, a series of tests are conducted to measure the negative stiffness experimentally and confirm the effect of the EATS in vibration isolation.

1. Introduction

Nonlinear passive isolators with high-static-low-dynamic stiffness characteristic, generally achieved by combining a positive stiffness spring and a negative stiffness springs, have received considerable attention in the past twenty years due to their excellent performance compared to linear vibration isolators [1–4]. Negative stiffness plays an important role in high-static-low-dynamic stiffness system and can be achieved by a number of ways. However, most of them are passive mechanism whose negative stiffness cannot be adjusted. For example, a common way to obtain negative stiffness in the research papers [5, 6] is using two oblique mechanical coil springs. With these two precompressed coil springs, a negative stiffness can be got in vertical direction but cannot be adjusted as there is no adjustment mechanism. A similar negative stiffness device realized by using the mechanical coil spring was presented by Meng et al. [7]. Besides, another way to achieve negative stiffness is utilizing structure buckling phenomena. In the paper given by Platus [8], the stiffness of a beam subjected to an axial load showed negative characteristic. Similarly, the studies in [9, 10] showed that the negative stiffness mechanism can be designed by using compressed Euler bulked beams. An impressive method to realize negative stiffness using cam-roller-spring mechanism can be found in [11, 12]. Furthermore, permanent magnets can also be utilized to obtain negative stiffness. The negative stiffness mechanism presented in [13] was conducted by using three permanent magnets arranged in an attracting configuration. In addition, another two types of negative stiffness mechanism made by permanent magnets can be found in [14, 15]. In the paper presented by Meng et al. [16], a negative stiffness spring was proposed by using disk springs, whose force characteristic in vertical direction was similar to that of the two oblique springs mechanism. Many other different types of passive nonlinear isolators have been discussed and compared comprehensively by Ibrahim in his review paper [17].

In general, passive nonlinear isolators are incapable of dealing with varying conditions such as changes of excitation frequencies or other system parameters. One common way to adjust the nonlinear isolator's properties is to change its stiffness. The positive stiffness variation has been well studied in many papers and a lot of configurations have been proposed, while the negative stiffness variation is not. To the best of our knowledge, the design and study of

variable negative stiffness are rarely reported. Only two ways have been found so far to realize variable negative stiffness: utilization of electromagnets [18–20] and application of actuator [21]. Zhou and Liu [18] and Francisco Ledezma-Ramirez et al. [19, 20] have presented a series of papers in which the negative stiffness is obtained by using two electromagnets and one (or two) permanent magnet. It works like the mechanism proposed by [13], but the negative stiffness can be changed by adjusting the input current. However, the characteristic of the magnet is very sensitive to the temperature and the demagnetization phenomenon will occur at high temperature. Thus, the isolator with magnets is not suitable for vibration isolation at high temperature. Unlike the way of using the electromagnets, Xu and Sun [21] proposed a theoretical model with adjustable negative stiffness by applying actuators to the traditional negative stiffness mechanism shown in [5, 6] to change the prestressed length of oblique springs. However, this regulating mode of the negative stiffness may be not very suitable for the practical application due to the empty trip phenomenon.

Although two ways have been proposed to realize variable negative stiffness, it is still too few for future application of variable negative stiffness and some new approaches should be studied. In this paper, a new approach is developed to achieve variable negative stiffness and applied in vibration isolation. The variable negative stiffness is created by an electromagnetic asymmetric tooth structure (EATS) and can be changed by adjusting the magnitude of the direct current. No magnet is used in the design so that the influence of the temperature on the effectiveness of the negative stiffness is very small. The magnitude of the negative stiffness is adjusted by the current; thus no auxiliary regulating mechanism is needed. It is not the intention here to address the advantage of the designed isolator compared with those impressing isolators proposed by [18–21] or how low frequency the designed isolator can work in. Rather the intention is to show a new way to achieve variable negative stiffness and validate it by simulation calculations and experimental tests.

The paper is organized as follows. Firstly, an electromagnetic vibration isolator is designed in Section 2. The electromagnetic force with negative stiffness is modeled theoretically and validated by finite element software. Secondly, in Section 3, the EATS is applied to vibration isolation and an electromagnetic vibration isolator is proposed. Thirdly, the experimental rig is built and the dynamic responses of the isolator in sweep and single frequencies are measured in Section 4. Finally, the conclusion is given in Section 5.

2. Configuration, Model, and Simulation of the EATS

2.1. Basic Configuration of the EATS. The idea of electromagnetic asymmetric tooth structure comes from the design of the traditional electromagnetic tooth structure (TETS), also called electromagnetic spring, which has been used in vibration absorption [22]. The axisymmetric schematic diagram of the TETS is shown in Figure 1(a), in which the blue arrows denote the magnetic lines. The stator and the active

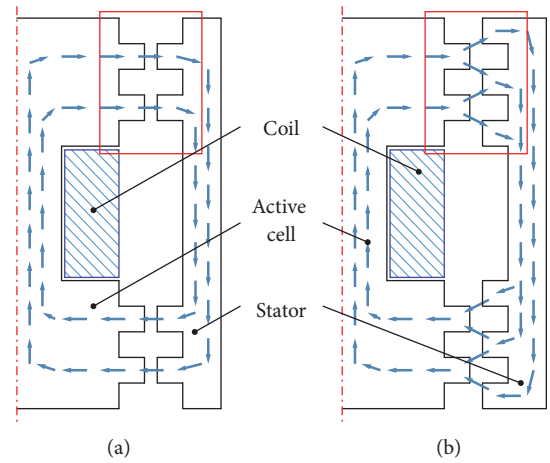

Figure 1: Axisymmetric schemes of (a) the traditional tooth structure and (b) the asymmetric tooth structure.

cell are made by electrical iron that has high permeability. The number of the active cell teeth is equal to that of the stator and all the teeth are arranged symmetrically. There will be a closed magnetic circuit existing in the tooth structure and all the magnetic lines from one active cell tooth flow into the opposite stator tooth when a constant direct current passes through the coil. If the active cell moves away from the stator in vertical direction, an electromagnetic force will be generated between tooth pairs to prevent this movement. Thus, the system behaves like a mechanical spring and has a positive stiffness near the equilibrium position.

Figure 1(b) shows the axisymmetric schematic diagram of the EATS. Different to the TETS, the number of the stators is two larger than that of the active cell and every active cell tooth is arranged between two stator teeth. Thus, the magnetic lines from one active cell tooth flow into two stator teeth and one active cell is applied by two electromagnetic forces in opposite directions. When the active cell stays at the equilibrium position, the overall electromagnetic force is zero and the system is quasi-stable. However, if the active cell moves away from the equilibrium position, there will be an electromagnetic force generated between the active cell and the stator to strengthen this movement and the system becomes unstable. Thus, the system behaves like an electromagnetic spring with negative stiffness.

2.2. Analytical Model of the Electromagnetic Force of the EAST

2.2.1. Equivalent Magnetic Circuit Model. It can be seen from Figure 1 that the EAST consists of four active cell teeth and six stator teeth, which means that eight tooth pairs should be considered in magnetic circuit modeling. In general, the magnetic resistance of the air gap is much larger than that of the magnetizer which is made by electrical iron; thus, the magnetic resistance of the active cell and stator is neglected in theoretical modeling. Figure 2 shows the equivalent magnetic circuit of EATS, where Λ is the magnetic conductance of the air gap and Φ is the corresponding magnetic flux.

For one of the air gaps, which is numbered 1, the magnetic coenergy is

$$W_1 = \frac{1}{2}\frac{NI}{2}\Phi_1 = \frac{(NI)^2 \Lambda_1}{8} \tag{1}$$

where N is the turns of the coil and I is the magnitude of the coil current.

The electromagnetic force can be derived by using virtual work principle

$$F_1 = -\frac{\partial W_1}{\partial x} = -\frac{(NI)^2}{8}\frac{\partial \Lambda_1}{\partial x} \tag{2}$$

where x is the relative displacement between the active cell and the stator.

Therefore, the overall electromagnetic magnetic force is

$$\begin{aligned} F &= -2\left(\frac{\partial W_1}{\partial x} - \frac{\partial W_2}{\partial x} + \frac{\partial W_3}{\partial x} - \frac{\partial W_4}{\partial x}\right) \\ &= -\frac{(NI)^2}{4}\left(\frac{\partial \Lambda_1}{\partial x} - \frac{\partial \Lambda_2}{\partial x} + \frac{\partial \Lambda_3}{\partial x} - \frac{\partial \Lambda_4}{\partial x}\right) \end{aligned} \tag{3}$$

2.2.2. Axial Electromagnetic Force of the EATS. The magnetic lines from every tooth of the active cell flow into the two stator teeth nearby; therefore, one negative stiffness mechanical unit consists of two different kinds of tooth pairs. The gap partitions of the two different tooth pairs are shown in Figure 3.

Figure 3(a) shows the situation that an active cell tooth moves close to a stator tooth, in which the solid line represents the initial location of the active cell tooth and the two-dot chain line represents the location of the active cell tooth with x displacement.

For the overlap section shown in Figure 4(a), the magnetic circuit is straight and the corresponding magnetic conductance Λ_a is

$$\Lambda_a = \frac{2\mu_0 \pi r x}{g} \tag{4}$$

where r is the radius of active cell and g is the width of air gap.

Different to that of the overlap section, the magnetic circuit of the edge section is elliptic. The short radius of elliptic circuit is l and the long radius of elliptic circuit is $g + \kappa l$, where the elliptic circuit coefficient κ is given as

$$\kappa = \frac{l}{g + l} \tag{5}$$

The differential sectional area of the edge circuit is

$$ds = 2\pi r \frac{dl + \kappa dl}{2} = \pi r (1 + \kappa)\, dl \tag{6}$$

and the corresponding average length is given by

$$l_m = g + \frac{\pi}{2} l \tag{7}$$

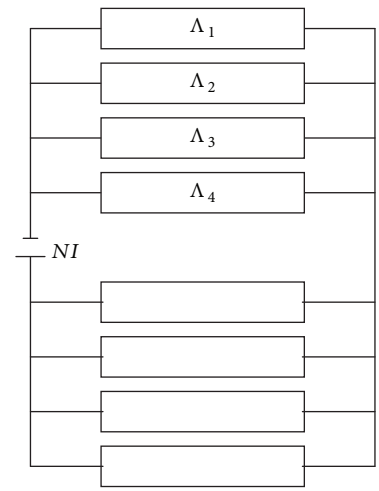

Figure 2: Equivalent magnetic circuit of EATS.

Combining (5)~(7) and considering the symmetry of magnetic circuit can give the magnetic conductance of the edge partition as

$$\begin{aligned} \Lambda_b = \Lambda_c &= \int \frac{\mu_0}{l_m} ds = \int_0^{w-x} \frac{\mu_0}{g + \pi l/2} \pi r (1 + \kappa)\, dl \\ &= \frac{2\mu_0 r}{\pi - 2}\left[\pi \ln \frac{g + w - x}{g} + (\pi - 4) \ln \frac{2g + \pi w - \pi x}{2g}\right] \end{aligned} \tag{8}$$

Thus, the overall magnetic conductance of the magnetic circuit shown as Figure 4(a) is

$$\begin{aligned} \Lambda_{e1} = \Lambda_a + \Lambda_b + \Lambda_c &= \frac{2\mu_0 \pi r x}{g} \\ &+ \frac{4\mu_0 r}{\pi - 2}\left[\pi \ln \frac{g + w - x}{g}\right. \\ &\left. + (\pi - 4) \ln \frac{2g + \pi w - \pi x}{2g}\right] \end{aligned} \tag{9}$$

Substituting (9) into (2) obtains the electromagnetic force F_{e1}

$$\begin{aligned} F_{e1} = -\frac{(NI)^2}{8}\frac{\partial \Lambda_{e1}}{\partial x} &= \frac{\pi \mu_0 r (NI)^2}{4}\left[-\frac{1}{g}\right. \\ &\left. + \frac{2}{\pi - 2}\left(\frac{1}{g + w - x} - \frac{4 - \pi}{2g + \pi w - \pi x}\right)\right] \end{aligned} \tag{10}$$

Figure 3(b) shows the situation that an active cell tooth moves away from a stator tooth, in which the solid line represents the initial location of the active cell tooth and the two-dot chain line represents the location of the active cell tooth with x displacement. Only elliptic circuits exist in this situation and the corresponding magnetic conductance is given by

$$\Lambda_a = \Lambda_b = \int_x^{w+x} \frac{\mu_0}{g + (\pi/2) l} \pi r \frac{g + 2l}{g + l} dl$$

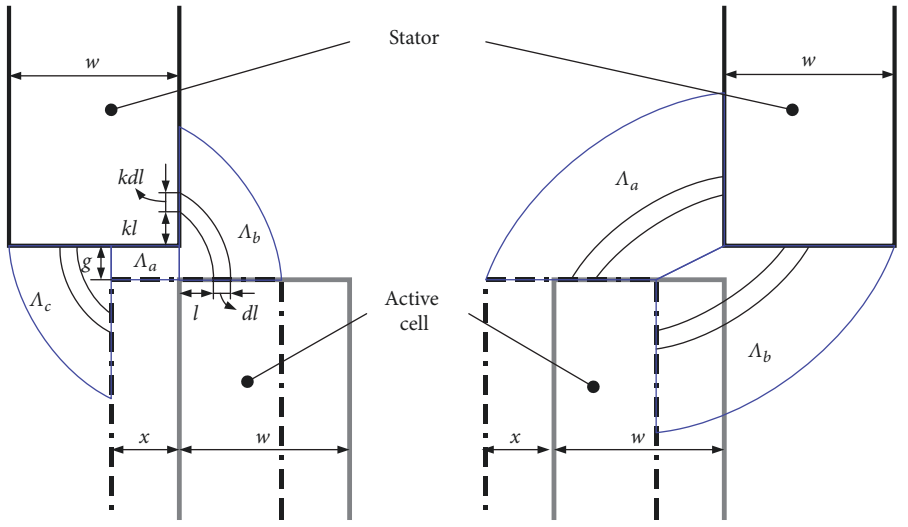

Figure 3: Air gap partition of a mechanical unit with negative stiffness.

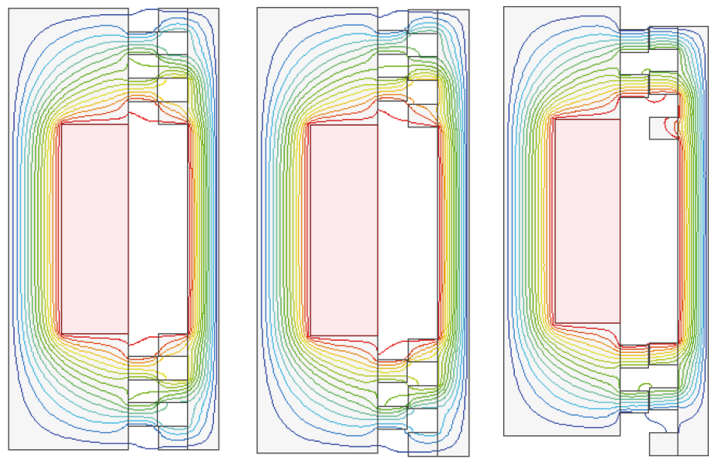

(a) 0 mm (b) 0.5 mm (c) 3.5 mm

Figure 4: Magnetic fields of EATS for different active cell positions for $I = 0.6$ A.

$$= \frac{2\mu_0 r}{\pi - 2}\left[\pi \ln\left(1 + \frac{w}{g + x}\right) + (\pi - 4)\ln\left(1 + \frac{\pi w}{2g + \pi x}\right)\right] \tag{11}$$

Therefore, the overall magnetic conductance of the magnetic circuit shown in Figure 3(b) is

$$\Lambda_{e2} = \Lambda_a + \Lambda_b = \frac{4\mu_0 r}{\pi - 2}\left[\pi \ln\left(1 + \frac{w}{g + x}\right) + (\pi - 4)\ln\left(1 + \frac{\pi w}{2g + \pi x}\right)\right] \tag{12}$$

and the electromagnetic force F_{e2} is

$$F_{e2} = -\frac{(NI)^2}{8}\frac{\partial \Lambda_{e2}}{\partial x} = \frac{\pi w \mu_0 r (NI)^2}{2(\pi - 2)}\left[\frac{1}{(w + g + x)(g + x)} - \frac{\pi(4 - \pi)}{(\pi w + 2g + \pi x)(2g + \pi x)}\right] \tag{13}$$

Combining (3), (10), and (13), the overall electromagnetic force of the EATS is obtained by

$$F = \operatorname{sgn}(x)\left\{\pi \mu_0 r (NI)^2\left[-\frac{1}{g}\right.\right.$$

Table 1: Simulation parameters.

Parameter	Value
Tooth width	4 mm
Tooth space	4 mm
Width of gap	0.3 mm
Coil current	0.6 A
Coil turns	190
Permeability material	DT4-C

$$+\frac{2}{\pi-2}\left(\frac{1}{g+w-|x|}-\frac{4-\pi}{2g+\pi w-\pi|x|}\right)\Bigg]$$
$$+\frac{2\pi w\mu_0 r\,(NI)^2}{\pi-2}\left[\frac{1}{(w+g+|x|)(g+|x|)}\right.$$
$$\left.-\frac{\pi(4-\pi)}{(\pi w+2g+\pi|x|)(2g+\pi|x|)}\right]\Bigg\} \quad (14)$$

where sgn(•) is the sign function.

2.3. Simulation of the EATS. In order to validate the negative stiffness of the EATS and demonstrate the correctness of the analytical electromagnetic force, a series of simulations of the EATS are conducted. Figure 4 shows the simplified simulation model and the distribution of the magnetic flux for different active cell positions for a current of 0.6 A. Table 1 depicts the parameters used in simulations by using finite element software.

When the active cell rightly stays at the equilibrium position, the magnetic field of the EATS is shown in Figure 4(a). The magnetic fluxes from every tooth of the active cell flow into two teeth of the stator; therefore, there are two forces which exist between one active cell tooth and two stator teeth. The overall electromagnetic force of the EATS is zero and the system is quasi-stable. When the active cell moves upwards 0.5 mm, shown in Figure 4(b), the distribution of the magnetic flux from one active cell tooth to two stator teeth is changed. The magnetic flux of the upper close stator tooth becomes larger and that of the lower close stator tooth is contrary; thus, the direction of the overall electromagnetic force is also upward, same as the moving direction of the active cell, and the system is unstable. When the active cell moves upwards 3.5 mm above the equilibrium position, it is interesting that the magnetic field of the EATS is similar to that of the traditional tooth structure with positive stiffness characteristic and detailed analysis can be found in [22].

Table 2 shows the parameters used in analytical calculation of the electromagnetic force. Substituting the parameters shown in Table 2 to (14) leads to the analytical electromagnetic force and the results are shown in Figure 5. Besides, the simulation results for various current are also plotted in Figure 5 to compare with the analytical solutions.

It can be seen from Figure 5 that the analytical solutions calculated by (14) match well with the simulation results. Furthermore, it is demonstrated that the EATS can provide an electromagnetic force with negative stiffness near the equilibrium position and the magnitude of the force can be changed by adjusting the coil current. Another important phenomenon which should be noted is that the electromagnetic force provided by the EATS has piecewise characteristic and the stiffness will become positive if the active cell has a large displacement.

Table 2: Parameters of analytical electromagnetic force.

Parameter	Value
μ_0	$4\pi \times 10^{-7}$
r	39.5 mm
N	190
I	0.5 A/0.6 A/0.7 A
g	0.3 mm
w	4 mm

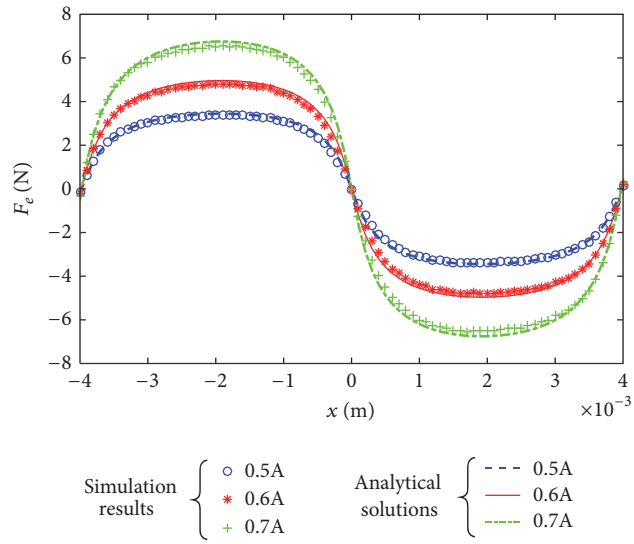

Figure 5: Electromagnetic force of the EATS for various current.

3. Application of the EATS

In an effort to capture the negative stiffness characteristic of the EATS in the following experimental tests, the EATS is applied to vibration isolation and an electromagnetic vibration isolator (EVI) is proposed in this section.

3.1. Basic Configuration of the EVI. The schematic structure and 3D configuration of the designed electromagnetic vibration isolator is depicted in Figure 6. Figure 7 shows the photograph of the components of the EVI. The isolator mainly includes two components: mechanical coil springs used to provide positive stiffness and electromagnetic asymmetric tooth structure used to provide negative stiffness. The mechanical springs consist of three types of coil springs, symbolized by k_{11}, k_{12}, and k_{13} separately. One mechanical spring denoted by k_{12} and four mechanical springs all denoted by k_{13} are employed to maintain the active cell at

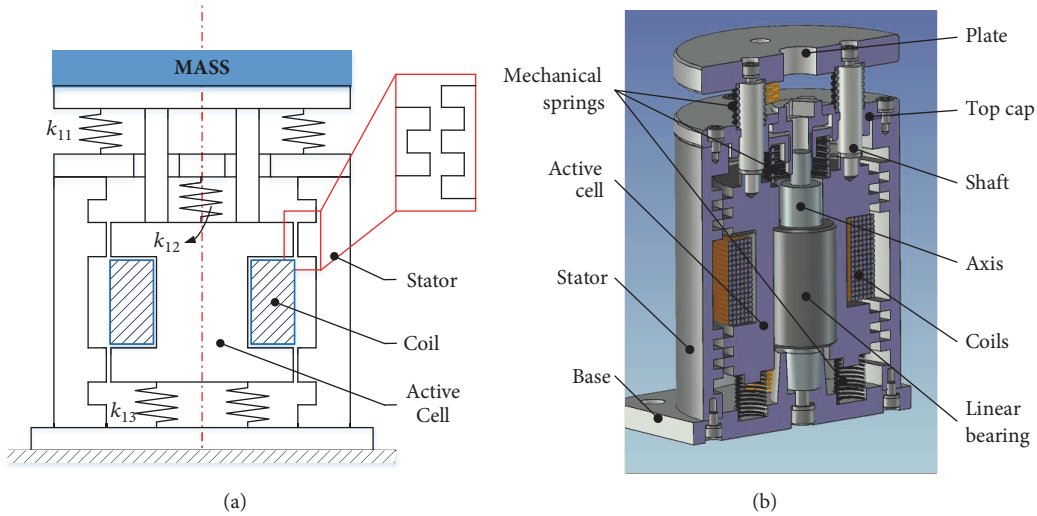

Figure 6: Scheme and 3D configuration of EVI: (a) schematic diagram and (b) 3D configuration.

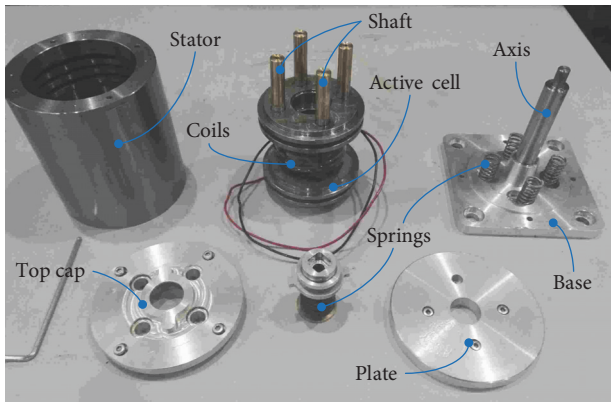

Figure 7: Photograph of the components of the EVI.

the desired position when no electric power is applied and no additional isolated mass is added. The mechanical coil springs symbolized by k_{11}, placed between the plate and the cylinder body, are only used to balance the additional mass and provide positive vertical stiffness in future application. A linear bearing is placed between the active cell and the axis for the purpose of maintaining the concentricity of the active cell and the stator. It should be noted that the static stiffness depends only on the mechanical coil springs, while the dynamic stiffness comes from the combined effect of the mechanical springs and the electromagnetic tooth structure.

It can be known from [23] that a mistuning mass will lead to a much more complex dynamic response of the system. Thus, a regulating mechanism of the active cell position, shown in Figure 8, is designed to solve this problem.

The regulating mechanism can adjust the position of the active cell by changing the precompression of the intermediate spring. When the position of the active cell needs to be adjusted, an adjusting knob is inserted into the screw thread mechanism and can be rotated clockwise or anticlockwise to adjust the upper end of the mechanical spring. It should be noted that the adjusting knob should be designed horizontally in future practical application for the reason that the isolated mass will be mounted on the plate.

3.2. Stiffness Characteristics of the EVI. Figure 9 depicts the force and displacement curves of the EATS for various current; meanwhile, the force characteristic curve of mechanical springs is also plotted for comparison. In the near area of the equilibrium position, the electromagnetic force provided by the EATS has a negative stiffness characteristic and the overall stiffness of the mechanical springs is reduced. The electromagnetic force becomes larger when the current increases. The overall force will be zero if the current increases to 1.1 A because the electromagnetic force is equal to the mechanical spring force. When the current exceeds 1.1 A, the overall force will have a negative stiffness characteristic near the equilibrium position and the active cell cannot be brought back to the equilibrium position by the mechanical springs which is quite unfavorable in practical application.

However, there are still some imperfect aspects of the design that should be noted. For example, the range of the negative stiffness is limited to (−2 mm, 2 mm), which is quite small compared with that of [18]. Moreover, the negative stiffness provided by the EATS has a very obvious nonlinear characteristic; thus, the dynamic behaviors of the isolator may be more complex than that of the equivalent linear one. In what follows, a series of experiments are conducted to measure the negative stiffness and explore the dynamic responses of the designed electromagnetic vibration isolator.

4. Experimental Studies

This section describes a series of experimental tests that were conducted to validate the negative stiffness characteristic of the EATS and investigate the isolation performance of the EVI with or without excitation current. Two experimental tests were mainly performed: (i) frequency sweeps in the base

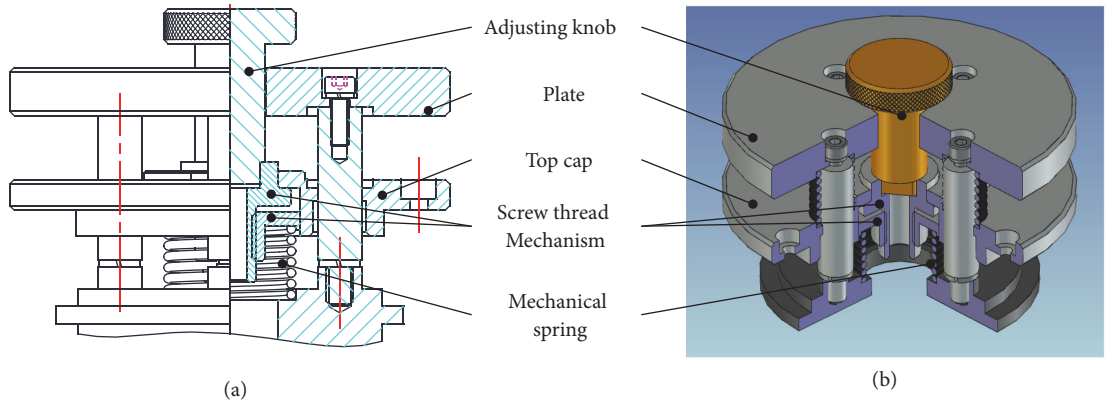

Figure 8: Regulating mechanism of active cell position.

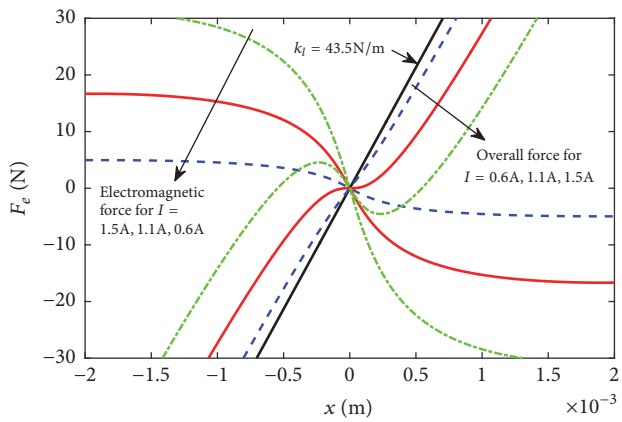

Figure 9: Force and displacement curves of the EATS for various current.

excitation frequency while holding base harmonic excitation velocity constant and (ii) isolation performances of the EVI system under single frequency harmonic excitation.

In this section, a numerical simulation corresponding to the experimental test is also carried out for two reasons: (i) supporting the experimental results and (ii) quantifying the influence of the current on the damping ratio due to the imperfect fabrication.

A simple analysis is conducted here to show how the numerical results are obtained. Assuming the vertical base excitation is $x_e = X_e \cos(\omega_e t)$, dynamic equation of the isolation system can be written as

$$m\ddot{x}_t + c(\dot{x}_t - \dot{x}_e) + k_l(x_t - x_e) + F = 0 \tag{15}$$

where x_t is the displacement response of the isolated mass, c is the damping, and F is the electromagnetic force which can be obtained from (14). We introduce the nondimensional parameters

$$y = \frac{(x_t - x_e)}{(X_e\omega)},$$

$$\zeta = \frac{c}{2m\Omega},$$

$$\omega = \frac{\omega_e}{\Omega},$$

$$\tau = \Omega t,$$

$$\Omega^2 = \frac{k_l}{m} \tag{16}$$

Equation (15) can be rewritten in nondimensional form as

$$y'' + 2\zeta y' + y + \frac{\widehat{F}}{X_e\omega k_l} = \omega\cos(\omega\tau) \tag{17}$$

where $\widehat{F}$ is the nondimensional form of (14). In the numerical analysis, only the primary resonance case is considered; thus, the solution of (17) can be assumed as $Y\cos(\omega\tau + \theta)$. The transmissibility of the isolation system corresponding to (17) can be derived as

$$T = \sqrt{1 + \omega^2 Y^2 + 2\omega Y\cos\theta} \tag{18}$$

Based on the above analysis, the numerical transmissibility results can be obtained by the fourth-order Runge-Kutta method and the fast Fourier transform.

Figure 10 shows the experimental setup and schematic diagram used in experimental tests. The isolator was powered by a DC power source and harmonically excited by an ES-10-240 shaker produced by Dongling Vibration Test Instrument Co., Ltd., China. The accelerations of the base excitation and the isolated mass were measured by two CA-YD-127 acceleration transducers produced by Sinocera Piezotronics Inc., China. A PC connected with a 3053-B data acquisition produced by Brüel & Kjær was used to collect and process acceleration response signals. In addition, there are several important points needed to be addressed. First of all, the active cell of the isolator was made by electrical pure iron and can be regarded as the isolated mass; thus, no additional isolated mass was mounted on the isolator and no mechanical spring denoted by k_{11} was placed between the plate and the top cap. Furthermore, when the DC power source was turned off, there was no electromagnetic stiffness and only

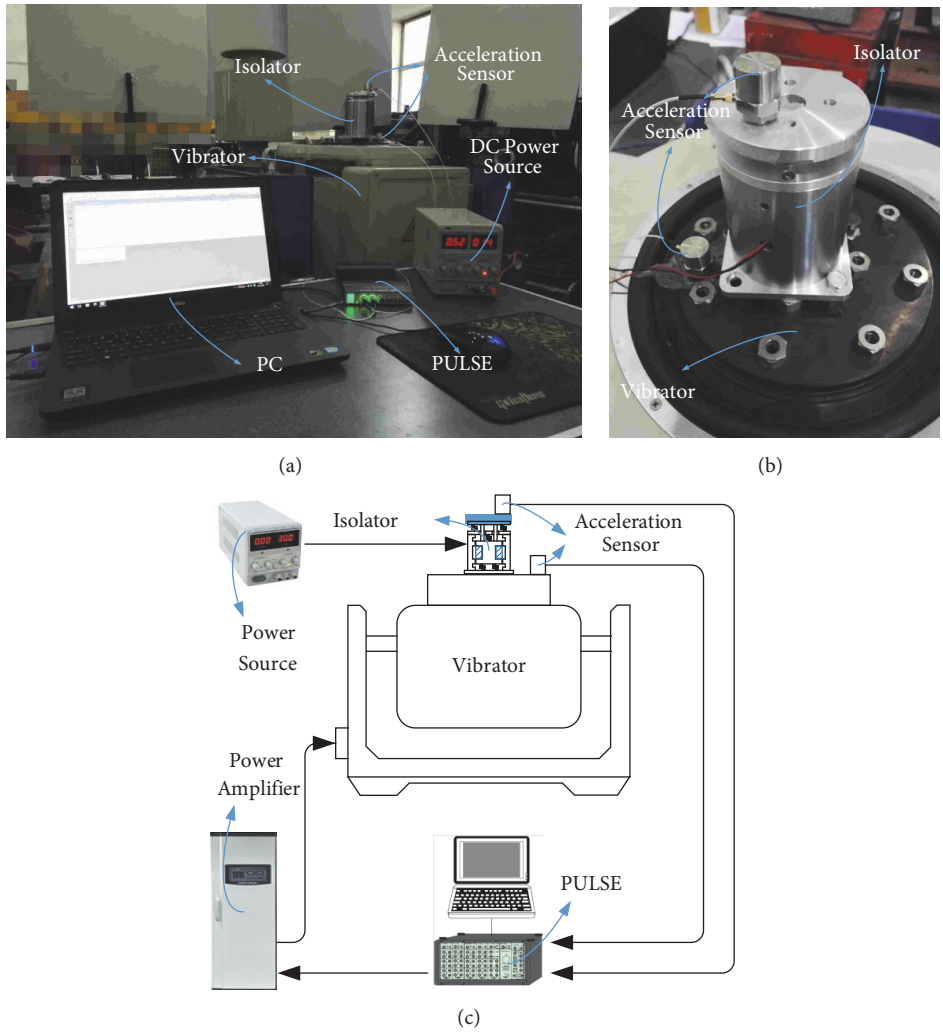

FIGURE 10: Experimental setup used in experimental tests: (a) primary equipment, (b) test rig, and (c) schematic diagram.

the mechanical springs worked. At last, compared with the displacement, the amplitude of the velocity was much easier to hold. Therefore, the amplitude of velocity was holding constant during the upward frequency sweep experiments. The frequency of the base excitation linearly varied from 5 Hz to 60 Hz in 10 seconds.

In Section 2, the analytical electromagnetic force is shown as (14). In order to calculate the negative stiffness near the equilibrium position, a third-order polynomial is applied to fit the theoretical results and the linear term of the fitting polynomial is the negative stiffness. Therefore, the theoretical resonance frequency of the isolation system can be calculated by

$$f_t = \frac{1}{2\pi}\sqrt{\frac{k_l + k_n}{m}} \tag{19}$$

where m is the isolated mass and k_n means the linear term of the negative stiffness. In the experiment, the isolated mass is 2.04 kg, which consists of four parts: the active cell, the shaft, the plate, and the acceleration transducer. The overall stiffness of the mechanical springs, k_l, is 43.5 N/mm.

Experimental acceleration and transmissibility curves from frequency sweeps are depicted in Figure 11, in which I is the magnitude of the current applied into the isolator. The velocity is 3.2×10^{-3} m/s which can be calculated by dividing the acceleration by the circular frequency. Besides, the numerical transmissibility results for various magnitudes of the current are also plotted in Figure 11(b), in which the asterisks represent the numerical results for damping ratio $\zeta = 0.04$ and the circles refer to the numerical results whose damping ratio is almost the same as that of the experimental results. It should be pointed out that the damping ratio of 0.04 is not obtained by experimental measurements but rather by numerical calculations. When the DC power is turned off, the electromagnetic asymmetric tooth structure does not work and the system can be regarded as a linear system. If the damping ratio is 0.04, the numerical results of the linear system compare well with that measured by experimental tests for no current. Thus, the damping ratio in experimental tests can be regarded as 0.04 to a certain

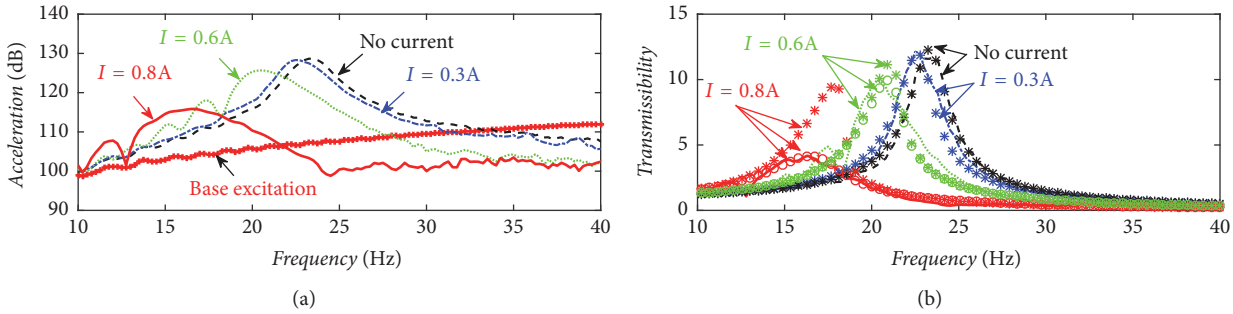

Figure 11: Experimental acceleration and transmissibility curves from frequency sweeps: (a) acceleration response and (b) transmissibility.

Table 3: Comparison of the theoretical resonance frequency and the experimental resonance frequency for various current.

Current (A)	Theoretical resonance frequency (Hz)	Experimental resonance frequency (Hz)	Error ratio (%)
0	23.24	23.25	0.04
0.3	22.51	22.50	0.04
0.4	21.93	22.00	0.32
0.5	21.16	21.25	0.42
0.6	20.17	20.25	0.40
0.7	18.94	19.25	1.61
0.8	17.41	17.00	2.41

degree. It can be seen that the experimental results compare well with the numerical results when the magnitude of the applied current is 0.3 A. However, when the magnitude of the current increases to 0.6 A, the peak transmissibility of the experimental results is a little lower than that of the numerical results; this is because that a radial electromagnetic force exists between the active cell and the stator due to the imperfect concentricity and it increases the damping force between the top cap and the shaft. The green circles represent the numerical results for $\zeta = 0.045$. In this case, the peak transmissibility of the numerical simulation is almost the same as that of the experimental measurement. Similar but more obvious phenomenon can also be found in the case of $I = 0.8$ A. In this case, the red circles refer to the numerical results for $\zeta = 0.09$. It should also be noted that the comparison of the numerical results and the experimental results is not very good at some frequencies. It is probably because that some other kinds of damping forces exist in the isolation system, such as the damping force inside the linear bearing when the current is being applied.

It can be known from Figure 11 that the experimental resonance frequency of the linear case is 23.24 Hz, which is identical with the theoretical result corresponding to (19). After applying a current of 0.3 A to the system, the EATS works and there is a negative stiffness to weaken the mechanical stiffness. Therefore, the experimental resonance frequency is reduced to 22.50 Hz, which is consistent with the theoretical result, 22.51 Hz. It can also been known from Figure 11 that the resonance frequency becomes smaller as the current increases. This is because a higher current leads to a larger negative stiffness and a smaller overall stiffness.

Table 3 gives the detailed comparison of the theoretical resonance frequency and the experimental resonance frequency for various current. The error ratio is defined as

$$e = \frac{|f_t - f_m|}{f_m} \times 100\% \tag{20}$$

where f_m is the experimental resonance frequency. From Table 3, it can be known that the theoretical frequencies for various current compare well with the measured results.

The analysis in Table 3 has confirmed that the derived analytical electromagnetic force is accurate enough and the proposed EATS is able to provide a variable negative stiffness near the equilibrium position. Another phenomenon which should be noted is that the isolation performance of the isolator with current is better than that of the isolator without current in low frequency range. In order to show this phenomenon better, the isolation response of the isolator with and without the current under single frequency harmonic excitation was measured. Considering the response curves shown in Figure 11, 23 Hz and 34 Hz were taken as the test frequency separately.

When the excitation frequency of the system is 23 Hz, the measured acceleration results of the isolator are shown in Figure 12. For better comparison of the isolation performance, base excitation curve is also plotted. When the DC power is turned off, the amplitude of the acceleration of the isolator is much larger than that of the base excitation. This is because the excitation frequency of 23 Hz is close to the resonance frequency of 23.25 Hz. After turning on the DC power, it is interesting to find out that the acceleration amplitude of the isolator at this frequency reduces from 30.341 m/s^2 to 3.495 m/s^2. Thus, the maximum displacement reduces

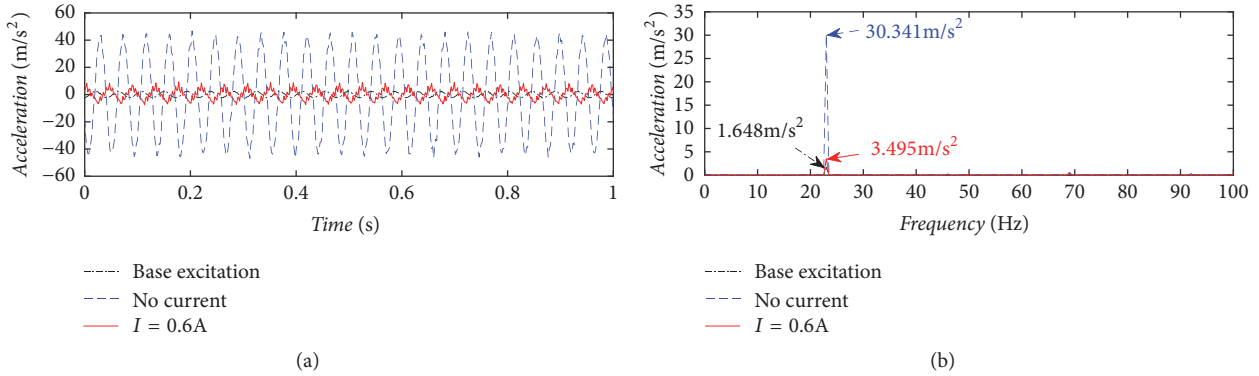

Figure 12: Isolation performance of the isolator for a base excitation frequency of 23 Hz: (a) time domain and (b) frequency domain.

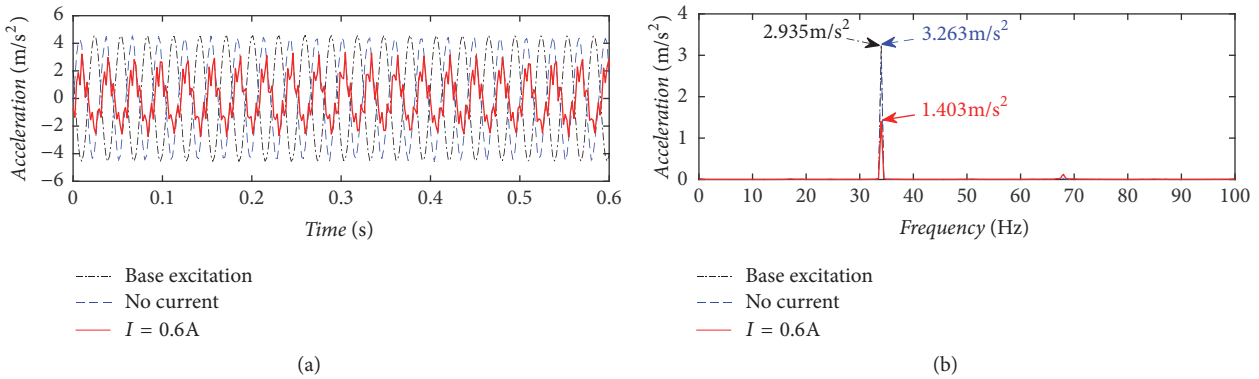

Figure 13: Isolation performance of the isolator for a base excitation frequency of 34 Hz: (a) time domain and (b) frequency domain.

from 1.45 mm to 0.17 mm and the isolation performance becomes much better than that of the former case. Similar phenomenon can be observed in the experimental tests at the frequency of 34 Hz, shown in Figure 13. At this frequency, the acceleration magnitude of the isolator without current applied is almost equal to that of the base excitation and the isolator has no vibration isolation effect. However, when a current of 0.6 A is applied to the isolator, there is an acceleration magnitude reduction of 1.860 m/s^2 at this frequency. This is because the negative stiffness provided by the EATS weakens the overall mechanical stiffness; therefore, both the resonance frequency and the initial isolation frequency become lower.

The above investigation has confirmed the variable negative stiffness provided by the EATS; however, there are still some unfavorable phenomenona which can be observed during the experimental tests. The first one is that the damping ratio becomes larger with the increase of the current. As we all know, a larger damping ratio is beneficial for the vibration isolation in low level frequency range; however, it is unfavorable for the vibration isolation in high level frequency range. The reason for this is that there is a contact friction between the top cap and the shaft. This is also why no static force measurements and sweep frequency experiments for large current are conducted in this paper. Another one is that there are some fluctuations in the measured results shown in Figure 11. This is because the base excitation provided by the shaker more or less has some small fluctuations in the initial sweep frequency range and the isolator amplifies such fluctuations in the low level frequency range.

5. Conclusions

This paper mainly describes a new approach to achieve variable negative stiffness. The negative stiffness is realized by an electromagnetic asymmetric magnetic tooth structure and can be changed by adjusting the magnitude of the input direct current. Analytical electromagnetic force model of the EATS is built and then validated by comparing with the simulation results. An electromagnetic vibration isolator is designed using the EATS and tested by a series of dynamical experiments. During the experiments, the negative stiffness of the EATS can be changed by adjusting the current which leads to the variation of the resonance frequency. The results confirm the negative stiffness provided by the EATS and demonstrate that the theoretical resonance frequencies calculated by the derived electromagnetic force equation compare very well with the experimental resonance frequencies. For the current of 0.6 A, the resonance frequency of the isolator reduces from 23.25 Hz to 20.25 Hz, and the acceleration amplitude of the isolator reduces from 30.341 m/s^2 to 3.495 m/s^2 at the frequency of 23 Hz. It indicates that the negative stiffness provided by the EATS is beneficial for vibration isolation.

However, it should be pointed out that there are still several aspects which require further investigation. First of all, some other methods of maintaining the concentricity of the active cell and the stator should be explored to reduce the damping ratio. For example, the linear bearing can be replaced by the polytetrafluoroethylene slide bush. Moreover, the tooth parameters of the EATS should be further studied to achieve a wider negative stiffness region and a smaller nonlinearity. Last but not least, the isolation performance of the isolator in large displacement situation should be investigated because the current negative stiffness region is a little small for a practical application. When the displacement of the active cell is larger than 2 mm, the stiffness becomes positive. The effect of the piecewise stiffness on the dynamic response could be further studied to solve such problem.

Conflicts of Interest

The authors declare that there are no conflicts of interest regarding the publication of this paper.

Acknowledgments

This work was supported by the National Natural Science Foundation of China (no. 51775124).

References

[1] Y. Wang, S. Li, C. Cheng, and X. Jiang, "Dynamic analysis of a high-static-low-dynamic-stiffness vibration isolator with time-delayed feedback control," *Shock and Vibration*, vol. 2015, Article ID 712851, 19 pages, 2015.

[2] H.-J. Ahn, S.-H. Lim, and C. Park, "An integrated design of quasi-zero stiffness mechanism," *Journal of Mechanical Science and Technology*, vol. 30, no. 3, pp. 1071–1075, 2016.

[3] Z. Lu, Y. Tiejun, M. J. Brennan, Z. Liu, and L.-Q. Chen, "Experimental Investigation of a Two-Stage Nonlinear Vibration Isolation System with High- Static-Low-Dynamic Stiffness," *Journal of Applied Mechanics*, vol. 84, no. 2, Article ID 021001, 2017.

[4] T. D. Le and K. K. Ahn, "Experimental investigation of a vibration isolation system using negative stiffness structure," *International Journal of Mechanical Sciences*, vol. 70, pp. 99–112, 2013.

[5] A. Carrella, M. J. Brennan, T. P. Waters, and V. Lopes Jr., "Force and displacement transmissibility of a nonlinear isolator with high-static-low-dynamic-stiffness," *International Journal of Mechanical Sciences*, vol. 55, no. 1, pp. 22–29, 2012.

[6] Z. Lu, T. Yang, M. J. Brennan, X. Li, and Z. Liu, "On the Performance of a Two-Stage Vibration Isolation System Which has Geometrically Nonlinear Stiffness," *Journal of Vibration Acoustics*, vol. 136, no. 6, Article ID 064501, 2014.

[7] Q. Meng, X. Yang, W. Li, E. Lu, and L. Sheng, "Research and Analysis of Quasi-Zero-Stiffness Isolator with Geometric Nonlinear Damping," *Shock and Vibration*, vol. 2017, 9 pages, 2017.

[8] D. L. Platus, "Negative-stiffness-mechanism vibration isolation systems," in *Proceedings of the SPIE's International Symposium on Optical Science, Engineering, and Instrumentation, International Society for Optics and Photonics*, pp. 98–105.

[9] X. Huang, X. Liu, J. Sun, Z. Zhang, and H. Hua, "Effect of the system imperfections on the dynamic response of a high-static-low-dynamic stiffness vibration isolator," *Nonlinear Dynamics*, vol. 76, no. 2, pp. 1157–1167, 2014.

[10] X. C. Huang, X. T. Liu, and H. X. Hua, "Effects of stiffness and load imperfection on the isolation performance of a high-static-low-dynamic-stiffness non-linear isolator under base displacement excitation," *International Journal of Non-Linear Mechanics*, vol. 65, pp. 32–43, 2014.

[11] Z. Yan, B. Zhu, X. Li, and G. Wang, "Modeling and analysis of static and dynamic characteristics of nonlinear seat suspension for off-road vehicles," *Shock and Vibration*, vol. 2015, Article ID 938205, 13 pages, 2015.

[12] J. Zhou, Q. Xiao, D. Xu, H. Ouyang, and Y. Li, "A novel quasi-zero-stiffness strut and its applications in six-degree-of-freedom vibration isolation platform," *Journal of Sound and Vibration*, vol. 394, pp. 59–74, 2017.

[13] A. Carrella, M. J. Brennan, T. P. Waters, and K. Shin, "On the design of a high-static-low-dynamic stiffness isolator using linear mechanical springs and magnets," *Journal of Sound and Vibration*, vol. 315, no. 3, pp. 712–720, 2008.

[14] D. L. Xu, Q. P. Yu, J. X. Zhou, and S. R. Bishop, "Theoretical and experimental analyses of a nonlinear magnetic vibration isolator with quasi-zero-stiffness characteristic," *Journal of Sound and Vibration*, vol. 332, no. 14, pp. 3377–3389, 2013.

[15] Y. Shan, W. Wu, and X. Chen, "Design of a miniaturized pneumatic vibration isolator with high-static-low-dynamic stiffness," *Journal of Vibration and Acoustics*, vol. 137, no. 4, Article ID 045001, 2015.

[16] L. Meng, J. Sun, and W. Wu, "Theoretical design and characteristics analysis of a quasi-zero stiffness isolator using a disk spring as negative stiffness element," *Shock and Vibration*, vol. 2015, Article ID 813763, 19 pages, 2015.

[17] R. A. Ibrahim, "Recent advances in nonlinear passive vibration isolators," *Journal of Sound and Vibration*, vol. 314, no. 3–5, pp. 371–452, 2008.

[18] N. Zhou and K. Liu, "A tunable high-static-low-dynamic stiffness vibration isolator," *Journal of Sound and Vibration*, vol. 329, no. 9, pp. 1254–1273, 2010.

[19] D. Francisco Ledezma-Ramirez, N. S. Ferguson, M. J. Brennan, and B. Tang, "An experimental nonlinear low dynamic stiffness device for shock isolation," *Journal of Sound and Vibration*, vol. 347, pp. 1–13, 2015.

[20] D. F. Ledezma-Ramirez, N. S. Ferguson, and M. J. Brennan, "An experimental switchable stiffness device for shock isolation," *Journal of Sound and Vibration*, vol. 331, no. 23, pp. 4987–5001, 2012.

[21] J. Xu and X. Sun, "A multi-directional vibration isolator based on Quasi-Zero-Stiffness structure and time-delayed active control," *International Journal of Mechanical Sciences*, vol. 100, article no. 3024, pp. 126–135, 2015.

[22] X. Liu, X. Feng, Y. Shi, Y. Wang, and Z. Shuai, "Development of a semi-active electromagnetic vibration absorber and its experimental study," *Journal of Vibration and Acoustics*, vol. 135, no. 5, Article ID 051015, 2013.

[23] A. Abolfathi, M. J. Brennan, T. P. Waters, and B. Tang, "On the effects of mistuning a force-excited system containing a quasi-zero-stiffness vibration isolator," *Journal of Vibration and Acoustics*, vol. 137, no. 4, Article ID 044502, 2015.